Journal of Hydrology 573 (2019) 31–39

Contents lists available at ScienceDirect

Journal of Hydrology

journal homepage: www.elsevier.com/locate/jhydrol

Research papers

Hydrodynamics, erosion and accretion of intertidal mudflats in extremely shallow waters

Benwei Shi[a,b,*], James R. Cooper[c], Jiasheng Li[d], Yang Yang[a], S.L. Yang[a], Feng Luo[e], Zixian Yu[f], Ya Ping Wang[a,g,*]

[a] State Key Laboratory of Estuarine and Coastal Research, East China Normal University, Shanghai 200062, China
[b] State Key Laboratory of Marine Geology, Tongji University, Shanghai 200092, China
[c] Department of Geography and Planning, School of Environmental Sciences, University of Liverpool, Liverpool, UK
[d] Ministry of Education Key Laboratory for Coast and Island Development, Nanjing University, Nanjing 210093, China
[e] Jiangsu Key Laboratory of Coast Ocean Resources Development and Environment Security, Hohai University, Nanjing 210098, China
[f] Rudong Meteorology Bureau, Nantong 226400, China
[g] Laboratory for Marine Geology, Qingdao National Laboratory for Marine Science and Technology, Qingdao 266061, China

ARTICLE INFO

This manuscript was handled by G. Syme, Editor-in-Chief, with the assistance of Li He, Associate Editor

Keywords:
Extremely shallow water stages
Bed-level changes
Hydrodynamics
Sediment transport

ABSTRACT

Intertidal flats are shallow-water environments that undergo cyclical variations in water depth, leading to a frequent occurrence of extremely shallow water stages (ESWS; water depths < 0.2 m). However, relatively little is known about the hydrodynamic conditions and erosion–accretion processes during ESWS, because the water depth is too shallow to measure *in situ* sediment dynamic processes using traditional methods. To address this gap, based on *in situ* measurements with four advanced instruments, we quantified the hydrodynamic conditions, erosion and accretion during ESWS in calm weather conditions on a highly turbid intertidal flat in Jiangsu coast, China. Our results revealed that marked erosion and accretion occurred during ESWS at the flood and ebb tidal stages, respectively. The resulting bed-level changes were three times greater during ESWS than relatively deep water stages (RDWS; water depths > 0.2 m), and the rate of change was an order of magnitude faster than during RDWS. This larger and faster bed-level change occurred even though the ESWS duration only accounted for 10% of the entire tidal cycle. This result occurred because the bed shear stress due to combined current–wave action during ESWS, was, on average, two times higher than during RDWS at the flood stage causing more extensive erosion. Whereas during the ebb stage, this shear stress during ESWS was only half of that during RDWS resulting in greater accretion. The main implications of these results are that, because ESWS occur frequently (twice every tide) and are associated with large bed shear stress and bed-level changes, these conditions are likely to play an important role in morphological changes of intertidal flats. Our study shows that ESWS have a key influence on intertidal flat hydrodynamics and sediment dynamics. Thus our results are the basis for an improved understanding of the coastal morphodynamic processes on intertidal flats.

1. Introduction

Intertidal flats are generally broad, shallowly sloping, intertidal zones with fine-grained sedimentary deposits (Eisma, 1998). These flats are highly productive components of shelf ecosystems (Le Hir et al., 2000; Ysebaert et al., 2003; Balke et al., 2011; Suykerbuyk et al., 2016), supporting large numbers of invertebrates and fish (Barbier, 2013; Bouma et al., 2016), and playing a key role in recycling organic matter and nutrients from both terrestrial and marine sources (Kautsky and Evans, 1987; Meziane and Tsuchiya, 2000; Li et al., 2012). Thus, developing an in-depth understanding of the processes that drive the dynamics of intertidal flats is important for management strategies and engineer design. One particular area that requires further investigation is the hydrodynamic and sediment transport processes that occur during extremely shallow water stages (ESWS), defined in this study as stages of water depth (h) < 0.2 m.

Previous studies have focused primarily on relatively deep water stages (RDWS; defined here as h > 0.2 m), revealing that the non-linear interactions between waves and currents on intertidal flats are responsible for strong turbulent mixing in the bottom boundary layer (e.g., Dyer, 1989; Le Hir et al., 2000; MacVean and Lacy, 2014; Yang et al., 2016; Yu et al., 2017), sediment transport in the tidal water

* Corresponding authors at: State Key Laboratory of Estuarine and Coastal Research, East China Normal University, Shanghai 200062, China.
E-mail addresses: bwshi@sklec.ecnu.edu.cn (B. Shi), ypwang@nju.edu.cn (Y.P. Wang).

https://doi.org/10.1016/j.jhydrol.2019.03.065
Received 2 October 2018; Received in revised form 14 March 2019; Accepted 16 March 2019
Available online 18 March 2019
0022-1694/

column (e.g., Janssen-Stelder, 2000; Wang et al., 2012; Shi et al., 2016), and morphological evolution (e.g., Andersen et al., 2006; Shi et al., 2014; Hu et al., 2015). However, intertidal flats worldwide are predominately shallow-water environments. Flats experience regular temporal–spatial variations in water depth due to cycles of emergence and submergence, leading to the frequent occurrence of extremely shallow water conditions (Gao, 2010; Fagherazzi and Mariotti, 2012; Zhang et al., 2016). In general, every tide has two ESWS, which are the initial stage of the flood tide and the following ebb tide. In comparison with RDWS, the maximum or minimum suspended sediment concentration (SSC) and current velocity within an entire tidal cycle may occur during ESWS (Gao, 2010; Zhang et al., 2016). Although this stage can be very short (typically several minutes, but sometimes only several seconds) with an entire tidal cycle (Gao, 2010), there is considerable potential for sediment transport and erosion–accretion during ESWS (Downing et al., 1981; Wang et al., 2012; Shi et al., 2017). Therefore, ESWS might play a significant role in controlling the overall topography of intertidal flats (Fagherazzi and Mariotti, 2012). For example, ESWS may promote the formation and destruction of micro-topography, such as sand ripples and grooves (Zhang et al., 2016), further resulting in the formation and modification of larger geomorphic units (Zhou et al., 2014).

Our understanding of the potentially important role of ESWS in the dynamics of intertidal flats is limited, because field investigations of hydrodynamic and erosion–accretion processes during ESWS are rare (e.g., Gao, 2010; Zhang et al., 2016). The main reasons for this are twofold. First, the extensive field instrumentation needed to gain integrated measurements of hydrodynamics, erosion–accretion, and sediment transport processes during ESWS is technologically challenging (Williams et al., 2008; Fagherazzi and Mariotti, 2012; MacVean and Lacy, 2014). Secondly, there are few reliable numerical models for modeling sediment dynamic processes during ESWS, due to difficulties in obtaining solvable equations for the complex sediment exchange and strong turbulent mixing processes in these conditions.

Therefore, this paper examines how hydrodynamic conditions, SSCs, and bed erosion–accretion processes differ between ESWS and RDWS on a highly turbid intertidal flat off the Jiangsu coast, China. We present time-series field measurements of current velocities, waves, SSCs, and bed-level changes throughout a number of tidal cycles under calm weather conditions. These continuous measurements form the basis for evaluating the link between hydrodynamics and bed-level changes during ESWS. Our data provide new insights into the importance of ESWS in controlling bed erosion–accretion processes and highlight that ESWS are critical in driving morphological change on intertidal flats.

2. Study area

Our study site is located on the Rudong intertidal flat, Jiangsu coast, China. This area comprises the largest radial-shaped tidal sand ridge system on the Chinese continental shelf in the southwestern Yellow Sea (Fig. 1A). The study area is a well-developed intertidal flat with a gentle slope (0.018%–0.022%) and width of several kilometers in the seaward direction (Zhu et al., 1986; Wang and Ke, 1997). The intertidal flat is a macrotidal area with a semi-diurnal tide and mean tidal range of 3.9–5.5 m (Ren et al., 1985; Wang and Ke, 1997; Xing et al., 2012). The flat is highly turbid due to the abundant sediment supply from the Yangtze River and abandoned Yellow River (Fig. 1A). The study area experiences frequent variations in water depth, and ESWS occurs twice every tide and approximately four times each day. A small wave height of < 1 m generally characterizes the study area during normal weather, and the annual average wind speed is 4–5 m/s (Ren, 1986). The intertidal area is generally flat and has no obvious tidal creek near the study site (Fig. 1B). The surface sediments are mainly silt (8–63 μm) on the upper tidal flat and fine sand (63–125 μm) on the middle tidal flat (Wang and Ke, 1997).

3. Materials and methods

3.1. Field measurements

3.1.1. Data collection

The field campaigns were conducted from November 28 to December 2, 2016. All instruments were installed firmly on a custom-made frame with an open structure and two stainless steel legs (Fig. 2). The relative height above the bed and setup of the instruments are detailed in Fig. 2 and Table 1, respectively.

Near-bed turbulent boundary velocities were measured using a downward-looking 6 MHz Nortek Acoustic Doppler Velocimeter (ADV) (measurement accuracy of ± 1 mm/s; data output rate of 1–64 Hz) at a sampling frequency of 16 Hz in 5 min bursts (4096 points per 5 min time-series). The ADV was fastened to the custom-made frame with the probe head positioned 0.2 m above the bed (Table 1), and measured the 3D turbulent velocity at a standoff distance of just 0.15 m from the probe head (Fig. 2). Thus, the turbulent velocities were measured at a height of ~0.05 m above the bed surface. To measure the turbulent velocity, the probe must be submerged, meaning that measurements of current velocities could only be undertaken when the water depth was > 0.2 m (i.e., not during ESWS). In addition to measuring the turbulent velocity, the ADV probe recorded a time-series of distance (with an accuracy of ± 1 mm) between the probe head and the local bed surface at 1 Hz. As such, actual bed elevation changes could be extracted from the time-series (Andersen et al., 2007; Salehi and Strom, 2012). The accuracy of the ADV measurements is robust and has been tested extensively in the laboratory (Salehi and Strom, 2012) and in the field (Andersen et al., 2007; Wang et al., 2014; Shi et al., 2015).

To capture the current velocity during ESWS, an electromagnetic current meter (EMCM) was used because this instrument is not affected by blind measurement areas, has a very small measurement volume, and a small probe diameter (~3 cm). To measure the 2D current velocity as close to the bed as possible, the EMCM was deployed at a height of only 0.05 m above the bed and operated at a burst period of 30 s and sampling frequency of 2 Hz (Fig. 2; Table 1).

Wave height was measured at a sampling frequency of 4 Hz over a 256 s period using a SBE 26plus SEAGAUGE (*Wave and Tide Recorder*; accuracy of 0.01% of the full scale) (Table 1). The SBE 26plus was installed horizontally on the bed, and its pressure sensor was located 0.05 cm above the bed (i.e., as close to the bed as possible) to record waves during ESWS (Fig. 2). The SBE 26plus collected 1024 measurements per burst and the mean water level was obtained every 10 min (Table 1). On the intertidal flat, the wave period was generally 2–5 s, and thus each burst recorded > 100 waves for estimation of wave height and period.

An optical backscattering sensor (OBS-3A; self-recording turbidity–temperature monitoring instrument) was used to make *in situ* measurements of turbidity at a sampling frequency of 1 Hz, with its sensor facing outward at a height of 0.05 m above the bed (Table 1; Fig. 2). To calibrate the *in situ* turbidity measurements in the laboratory, *in situ* water samples were collected at the same height as the OBS-3A measurements on a small boat near the observation site.

3.1.2. Determination of ESWS duration and bed-level changes

The ADV probes were exposed to air and stopped working when the water depth was < 0.2 m. Thus, the ADV instrument could not record the time at which the water attained a zero depth or the distance between the ADV probe and bed surface at this time. Therefore a boat anchored near the observation site recorded this time using a watch and the distance using a ruler. For the initial stage of flood tide, the duration ($\Delta T_{F\text{-}i}$) and bed-level change ($\Delta D_{F\text{-}i}$) of ESWS for each tide were estimated as follows:

$$\Delta T_{F\text{-}i} = T_{F\text{-}i} - T_{f\text{-}b\text{-}i} \tag{1}$$

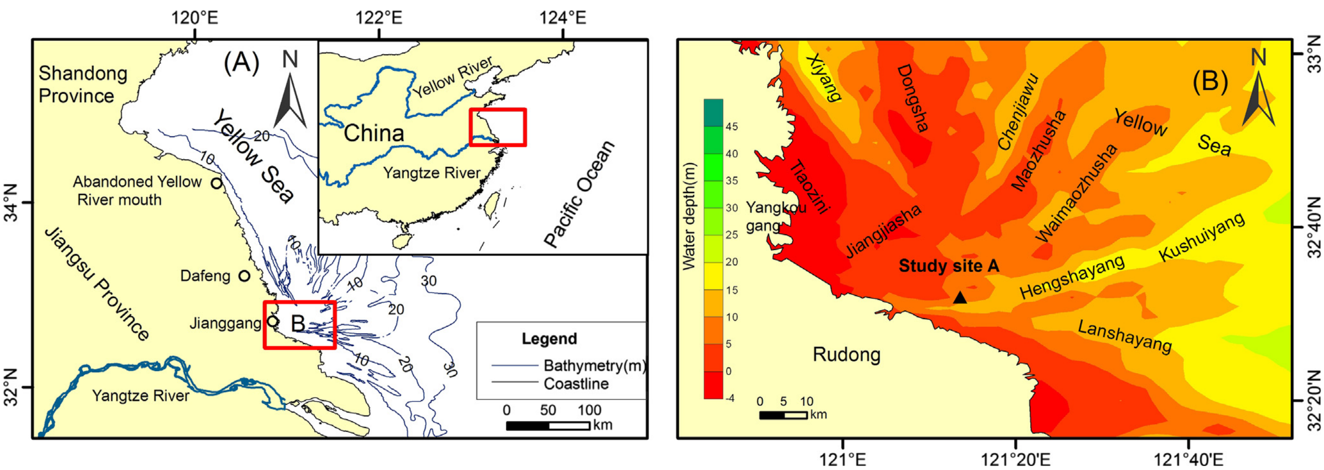

Fig. 1. Maps of the (A) Jiangsu coast and Yellow Sea, and (B) Rudong intertidal flat showing the study site A (black triangle). (For interpretation of the references to colour in this figure legend, the reader is referred to the web version of this article.)

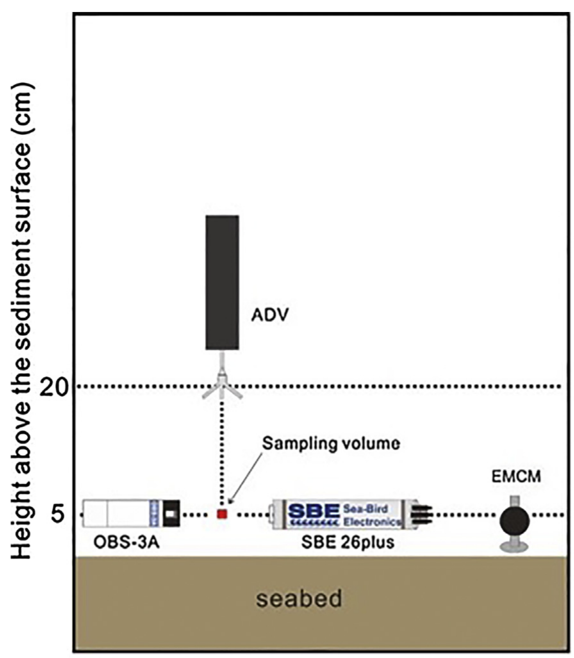

Fig. 2. 4 instrumentation.

$$\Delta D_{F\text{-}i} = D_{F\text{-}i} - D_{f\text{-}b\text{-}i} \tag{2}$$

where $T_{F\text{-}i}$ and $D_{F\text{-}i}$ are the time and distance, respectively, recorded when the water attained a zero depth at the initial stage of flood tide i, and $T_{f\text{-}b\text{-}i}$ and $D_{f\text{-}b\text{-}i}$ are the time and distance, respectively, recorded by the ADV at the first effective burst when $h \geq 0.2$ m during the flood tide stage.

For the post-ebb tide stage, the duration ($\Delta T_{E\text{-}i}$) and bed-level change ($\Delta D_{E\text{-}i}$) of ESWS for each tide were estimated as follows:

$$\Delta T_{E\text{-}i} = T_{e\text{-}b\text{-}i} - T_{E\text{-}i} \tag{3}$$

$$\Delta D_{E\text{-}i} = D_{e\text{-}b\text{-}i} - D_{E\text{-}i} \tag{4}$$

where $T_{e\text{-}b\text{-}i}$ and $D_{e\text{-}b\text{-}i}$ are the time and distance, respectively, recorded by the ADV in the last effective burst during the ebb stage during tide i (i.e., when $h \approx 0.2$ m), and $T_{E\text{-}i}$ and $D_{E\text{-}i}$ are the time and distance, respectively, recorded when the water attained a zero depth at the post-ebb tide stage during tide i.

3.2. Estimation of bed shear stress

The variation in bed shear stress within an entire tidal cycle was estimated using a current–wave interaction model. Specifically, the bed shear stress due to waves (τ_w) was calculated using the theory of wave orbital velocity (A1 in Appendix A) and wave friction (A3 and A4 in Appendix A), and the bed shear stress due to currents (τ_c) was calculated using the theory of bottom boundary layers (A5 and A6 in Appendix A) and friction velocity (u_*). The bed shear stress due to combined current–wave action (τ_{cw}) was calculated using the Grant and Madsen (1979) model (a classic current–wave interaction model; A7 in Appendix A), which has been widely used in the estimation of τ_{cw} (e.g., Lyne et al., 1990; Mellor, 2002; Feddersen et al., 2003; Zhang et al., 2004).

The bottom sediments were mainly very fine sand. At study site A the median grain size (d_{50}) was 113 μm during the field measurements. Thus, we determined the critical shear stress for erosion (τ_{cr}) using the Shields (1936) equation (B3, B4, and B5 in Appendix B), which has been applied by Miller et al. (1977), Soulsby (1997), and Yang et al. (2016). In this study, we used a value of 0.1 N/m^2 based on this median grain size.

4. Results

4.1. Wind, wave, and current data

During field measurements, offshore winds ranged in speed from 0.6 to 7.5 m/s, with a mean of 3.5 m/s (Fig. 3A), which was weaker than the annual mean wind speed of 4–5 m/s. Relatively weak winds

Table 1
Deployed field instruments and their operational settings.

Instruments	Height above the bed (cm)	Measured parameters	Burst intervals (s)	Sampling frequency (Hz)	Sampling numbers each burst
ADV	20	3D turbulent velocity	300	16	4096
OBS–3A	5	Turbidity, water depth	60	1	30
SBE 26 plus	5	Water depth, wave height and period	600	4	1024
EMCM	5	2D current velocity	30	2	30

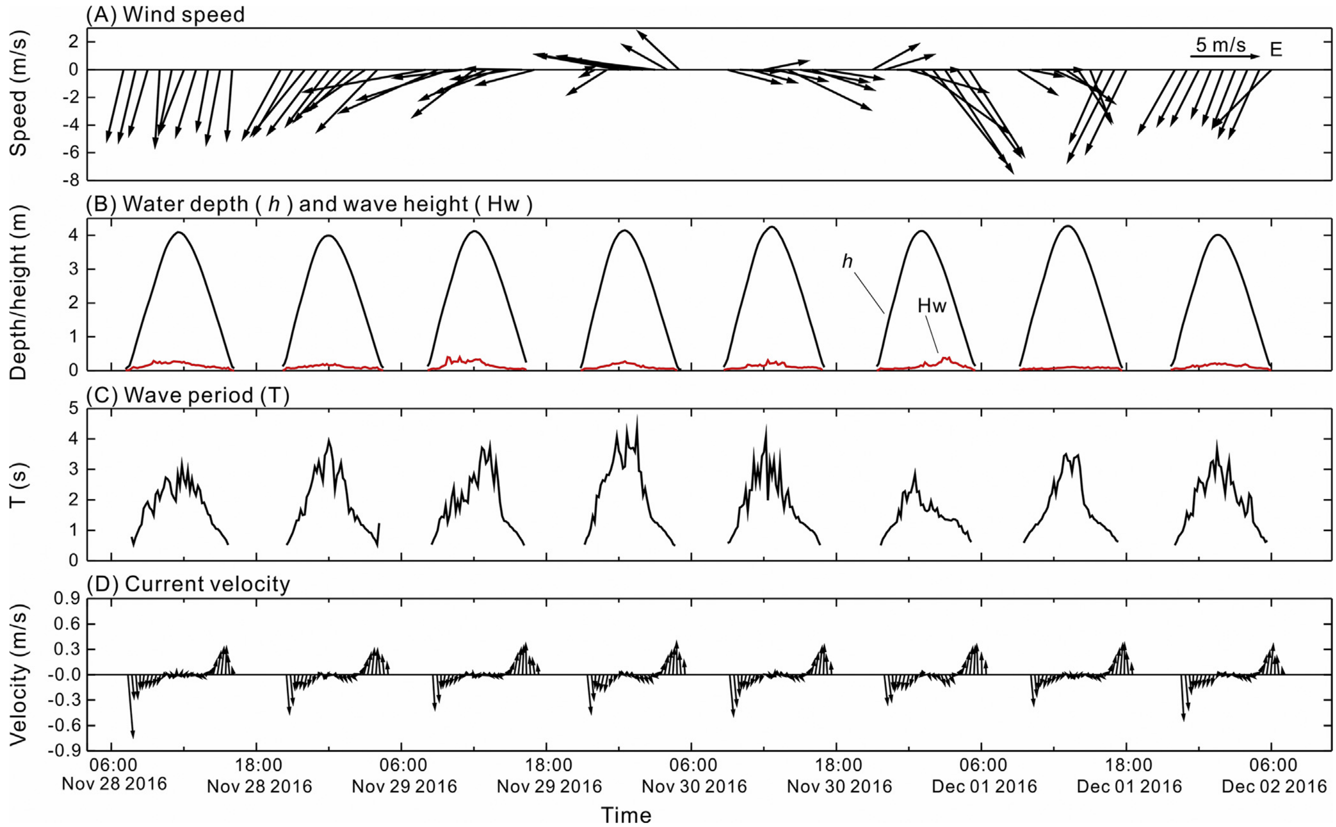

Fig. 3. Time-series of (A) wind speed, (B) water depth and wave height, (C) wave period, and (D) current velocity during the period of field measurements. The absence of data between tides indicates that the instrument sensors were exposed to air.

generated small waves during the field measurements. Thus, the maximum wave height was just 0.39 m (Fig. 3B). Wave height within an entire tidal cycle tended to be largest at the high water level and smallest at the low water level (Fig. 3B). The wave height was at its minimum during ESWS (Fig. 3B), perhaps due to the positive relationship between wave height and water depth.

Wave period and water depth showed the same temporal pattern. The maximum wave period was only 4.3 s, which tended to occur at high water levels, and the minimum (~1 s) occurred at ESWS during each tide (Fig. 3B–C).

Current velocity was rotational for the entire tidal cycle (Fig. 3D). The maximum current velocity occurred during ESWS in the initial flood stage (0.1–0.59 m/s), in an onshore direction (towards the south), and was greater than the current velocity during ESWS in the post-flood stage when the current direction switched to offshore (Fig. 3D). The current during RDWS tended to have an onshore direction in the flood stage, offshore direction in the ebb stage, and a smaller velocity than during ESWS in the initial flood stage (Fig. 3D).

4.2. Bed shear stresses

4.2.1. Shear stress due to waves (τ_w) and currents (τ_c)

The τ_w values varied little within a tidal cycle (0.01–0.15 N/m^2; Fig. 4B; Table 2) as a result of weak winds and small wave heights (Fig. 3B) under the calm weather conditions. The τ_w values during ESWS were comparable with those during RDWS (Table 2). The maximum τ_c value occurred during ESWS in the flood stage (Fig. 4B). The average τ_c during ESWS in the flood stage (0.30–0.64 N/m^2) was several times greater than during ESWS at the corresponding ebb stage (0.07–0.16 N/m^2), and was also greater than the average value during a RDWS in a corresponding tide (0.11–0.13 N/m^2) (Table 2).

4.2.2. Shear stress due to combined current–wave action (τ_{cw})

The maximum τ_{cw} value within a tidal cycle occurred during ESWS in the flood stage (Fig. 4B), and the average τ_{cw} during these stages ranged from 0.36 to 0.70 N/m^2 and was greater than τ_{cr} (0.1 N/m^2). In contrast, the average τ_{cw} during ESWS at the corresponding ebb stage ranged from 0.03 to 0.09 N/m^2 and was less than the average τ_{cr} (Fig. 4B). For RDWS, the average τ_{cw} varied little, ranging from 0.12 to 0.14 N/m^2, and was slightly greater than the average τ_{cr}.

4.3. Suspended sediment concentration

The average SSC during ESWS at the flooding stage (0.69 kg/m^3) was two times higher than at the ebb stage (0.33 kg/m^3; Table 2; Fig. 4C). In contrast, the average SSC during RDWS was lower than during ESWS at the corresponding flood stage and was higher than at the corresponding ebb stage (Table 2; Fig. 4C).

4.4. Duration of ESWS and RDWS

The duration of ESWS at the ebb stage (~30 min) was 1.5 times longer than that at the corresponding flood stage (~22 min), and the duration of ESWS only accounted for 10% of the entire tidal cycle (Table 3). In contrast, the duration of RDWS was 457 min on average, which was almost nine times longer than the average total duration (52 min) of ESWS. Thus, RDWS accounted for 90% of the entire tidal cycle (Table 3).

4.5. Bed-level changes

During the entire field campaign the distance from the ADV probe to the bed surface ranged from 280 to 285 mm, indicating that the overall bed-level change was just −5 mm (negative denoting erosion)

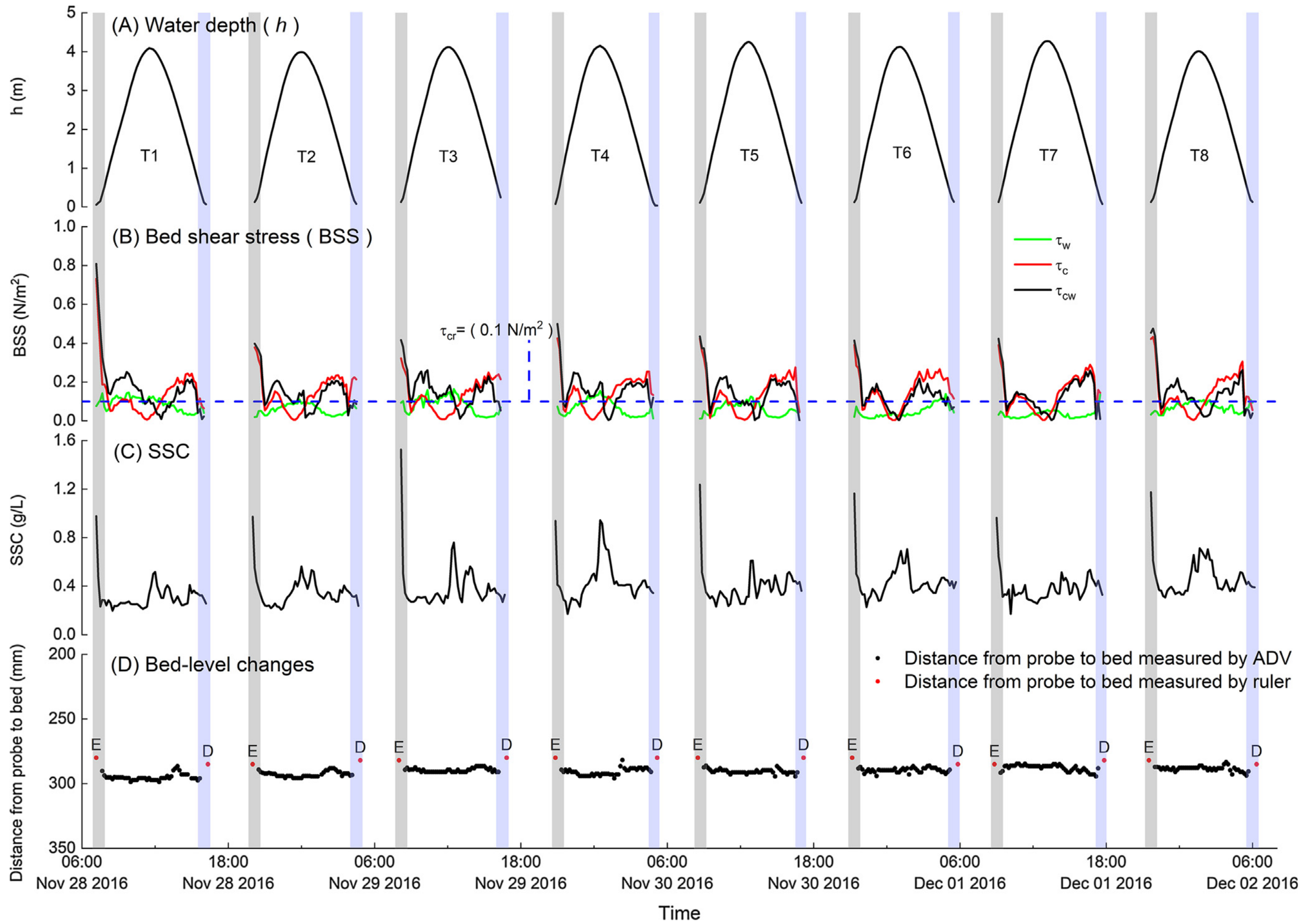

Fig. 4. Time-series of (A) water depth, (B) bed shear stress (τ_c, τ_w, and τ_{cw}), (C) suspended sediment concentration (SSC), and (D) bed-level changes. In (B), τ_c, τ_w, τ_{cw}, and τ_{cr} denote bed shear stress due to currents, waves, combined current–wave action, and critical bed shear stress for bottom sediments, respectively. In (D), gray bars indicate erosional phases of ESWS in the initial flood tide stage (denoted by E) and light blue bars indicate depositional phases of ESWS at the post-ebb tide stage (denoted by D). (For interpretation of the references to colour in this figure legend, the reader is referred to the web version of this article.)

(Fig. 4D). The bed-level change during ESWS was much greater than that during RDWS (Table 3; Fig. 4D). Erosion occurred during ESWS at the flooding stage of the tide, with an average magnitude of −7.4 mm (−4.2 to −10.3 mm) per tide at an average rate of −0.4 mm/min (−0.2 to −0.5 mm/min; Table 3). In contrast, accretion occurred during ESWS in the ebb stage, and the rate of this accretion was comparable to that of erosion, with the average amount being +9.2 mm (+4.4 to +14.5 mm; positive denoting accretion) per tide at an average rate of +0.3 mm/min (+0.1 to +0.5 mm/min; Table 3). However the rate of bed-level change for RDWS was much lower, with an average amount of −2.5 mm (+3.5 to −7.0 mm) per tide at an average rate of -0.6×10^{-2} mm/min ($+1 \times 10^{-2}$ to -2×10^{-2} mm/min; Table 3). Therefore, the magnitude of bed-level change during ESWS was three times greater than that during RDWS, and its rate was an order of magnitude higher, despite ESWS making up just 10% of the tidal cycle (Table 3).

5. Discussion

Our results reveal that strong erosion and weak accretion occurred

Table 2
Comparison of bed shear stress due to wave (τ_w), current (τ_c), and combined current–wave action (τ_{cw}), and SSCs and bed-level changes at water depths (h) of < 0.2 m (ESWS) and > 0.2 m (RDWS).

Tides	τ_w on average (N/m^2)			τ_c on average (N/m^2)			τ_{cw} on average (N/m^2)			SSC on average (kg/m^3)		
	ESWS		RDWS	ESWS		RDWS	ESWS		RDWS	ESWS		RDWS
	Flood	Ebb		Flood	Ebb		Flood	Ebb		Flood	Ebb	
T1	0.08	0.06	0.09	0.64	0.07	0.12	0.70	0.03	0.13	0.56	0.27	0.30
T2	0.02	0.07	0.06	0.37	0.16	0.13	0.36	0.09	0.14	0.58	0.27	0.34
T3	0.09	0.05	0.08	0.30	0.12	0.12	0.38	0.08	0.13	0.78	0.35	0.36
T4	0.06	0.04	0.07	0.40	0.13	0.13	0.45	0.09	0.14	0.51	0.35	0.43
T5	0.01	0.04	0.06	0.40	0.08	0.13	0.40	0.04	0.13	0.80	0.34	0.37
T6	0.05	0.06	0.04	0.35	0.12	0.11	0.37	0.08	0.12	0.74	0.36	0.42
T7	0.05	0.09	0.03	0.33	0.15	0.13	0.37	0.05	0.13	0.76	0.30	0.36
T8	0.04	0.10	0.07	0.42	0.07	0.13	0.45	0.04	0.14	0.85	0.37	0.45

Table 3
Comparison of bed-level change (BLC) and duration for an entire tidal cycle at water depths (h) of < 0.2 m (ESWS) and > 0.2 m (RDWS). Also shown are their percentage (%) duration relative to the entire tidal cycle and the rate of bed-level change (mm/min).

Tides	Entire tidal cycle		ESWS								RDWS			
	Duration (min)	BLC (mm)	Duration (min)		%		BLC (mm)		Rate (mm/min)		Duration (min)	%	BLC (mm)	Rate ($\times 10^{-2}$, mm/min)
			Flood	Ebb	Flood	Ebb	Flood	Ebb	Flood	Ebb				
T1	526	−5	19	32	3.6	6.1	−10.3	+11.0	−0.5	+0.3	475	90.3	−5.7	−1.0
T2	506	+3	18	28	3.6	5.5	−4.2	+11.4	−0.2	+0.4	460	90.9	−4.2	−1.0
T3	500	+2	20	35	4.0	7.0	−7.4	+11.0	−0.4	+0.3	445	89.0	−1.6	−0.4
T4	508	0	21	32	4.1	6.3	−9.4	+9.4	−0.4	+0.3	455	89.6	0.0	0.0
T5	513	0	17	31	3.3	6.0	−7.5	+14.5	−0.4	+0.5	465	90.7	−7.0	−2.0
T6	510	−5	23	33	4.5	6.5	−8.3	+4.4	−0.4	+0.1	454	89.0	−1.1	−0.2
T7	510	+3	24	34	4.7	6.7	−6.7	+6.2	−0.3	+0.2	452	88.6	+3.5	+1.0
T8	500	−3	19	31	3.8	6.2	−5.1	+5.6	−0.3	+0.2	450	90.0	−3.5	−1.0

"−" denotes erosion and "+" denotes accretion.

during ESWS at the flood and ebb stages of a tide, respectively, and relatively weak erosion occurred during RDWS in almost all tidal cycles (Table 3; Fig. 4D). This difference can be explained by the theory of sediment erosion–accretion (Appendix B; Winterwerp and van Kesteren, 2004) and the contrast in bed shear stress between ESWS and RDWS. The average erosion flux (F_e) during ESWS in the flood stage was greater than that during RDWS because the average τ_{cw} during ESWS in the flood stage was two times higher than during RDWS in a corresponding tidal cycle (Table 2; Fig. 4B) and greater than τ_{cr}. In contrast, in the ebb stage, the average F_e during ESWS was zero (due to $\tau_{cw} < \tau_{cr}$) and the average depositional flux (F_d) was much greater than during RDWS, because the average τ_{cw} during ESWS was only half of the average τ_{cw} during RDWS (Table 2; Fig. 4B). The τ_{cw} values were much lower than τ_{cr} values during ESWS, resulting in greater accretion. This accretion occurred during periods of much higher near-bed SSCs than were observed during RDWS (Table 2), reflecting relatively weak hydrodynamic conditions.

A detailed comparison of the bed-level changes and durations of ESWS and RDWS showed that ESWS were characterized by much shorter duration (10% of the entire tidal cycle), and larger and faster bed-level changes (Table 3). Morphological changes are generally related to not only the magnitude of extreme events, but also the frequency of their occurrence (Wolman and Miller, 1960). Thus, when considering the effects of ESWS on geomorphic processes on the studied intertidal flat, we should note that, although short in duration, ESWS occur twice every tidal cycle and there are two daily tidal cycles at this site (e.g., Wang et al., 2012; Xing et al., 2012). Therefore, ESWS occurs frequently on the intertidal flat. Given this high frequency and that ESWS are marked by large values of bed shear stress, these conditions have an important influence on the morphological development of intertidal flats. To illustrate this, we estimated the annual net cumulative bed-level change induced by ESWS to be about +66 cm, whereas this is about −182 cm during RDWS. Therefore, ESWS play a significant role in the annual replenishment of sediments. Given that our field investigations were undertaken in calm weather conditions, we can infer that in rough or stormy weather conditions the magnitude of bed-level changes during ESWS could be even larger.

It is important to consider whether our results are site-specific or are applicable to other intertidal environments. Based on a limited number of previous studies, we suggest the latter is the case for the following reason. Surges or pulses in tidal velocity have been identified in association with high SSCs in ESWS in different types of intertidal flats, such as: (i) sandy and muddy coasts (e.g., Postma, 1967; Bayliss-Smith et al., 1979; Gao, 2010; Nowacki and Ogston, 2013; Zhang et al., 2016); (ii) different geomorphic units within intertidal systems, such as tidal creeks and runnels (Fagherazzi et al., 2008; Fagherazzi and Mariotti, 2012; Hughes, 2012); (iii) in a range of intertidal systems, such as channel–flat and salt marsh systems (Pethick, 1980; Wang et al., 1999; Nowacki and Ogston, 2013); and (iv) under a range of meteorological conditions, including calm and stormy weather (Wang et al., 1999; Zhang et al., 2016). These observations suggest that this velocity surging/pulsing is common during ESWS in almost all tidal cycles in intertidal environments worldwide. Furthermore, based on the results of Zhang et al. (2016), these surges can produce large bed shear stress (up to 1.5 N/m^2) at the beginning of the flood tide, which is an order of magnitude higher than the critical shear stress of sediments commonly found on intertidal flats. Therefore, it is reasonable to expect that this surge could re-suspend and transport a large amount of bottom sediment, resulting in erosion at the beginning of the flood tide. This inference is in agreement with the strong erosion observed during ESWS in our study.

Previous studies have been conducted on field measurement of ESWS (Zhang et al., 2016; Shi et al., 2017). For example, Shi et al. (2017) have estimated the bed-level changes of ESWS during windy weather conditions on the same intertidal flat as this study, but on a different section. Their results have showed that bed-level changes due to erosion under calm conditions were six times lower than those reported in Shi et al. (2017) (−14.7 mm in Shi et al. (2017) vs. −2.3 mm (this study)) while bed-level changes due to accretion was slightly higher under our calm conditions (+6.8 mm (this study) vs. +5.1 mm in Shi et al. (2017)). The reason is that this study was made under calm conditions, which representing a rather weak intertidal sediment dynamics, while the results in Shi et al. (2017) represented relative stronger hydrodynamics since the wind speed could reached up to 13.6 m/s (Shi et al., 2017), showing that weather conditions can be an important factor in determining the importance of ESWS in morphological changes.

The limitations of this study are that we lacked the field data needed to measure in big detail time series of bed-level change to study processes and mechanism of sediment erosion, accretion, transport, biogeochemical cycle and micro-topography formation during ESWS. Therefore, the further avenues of research on sedimentary processes and hydrodynamics during ESWS should focus on the following: (1) spatial comparisons of sediment transport processes during ESWS in the subtidal, middle, and high intertidal zones. Hydrodynamics in these zones may differ greatly during ESWS compared with other periods, driving morphological change; (2) a comparison of sedimentary processes during ESWS in microtidal, mesotidal, and macrotidal intertidal flats, sheltered and exposed intertidal flats, and under calm and stormy weather conditions. For example, our study was performed under weak wind conditions, and there will likely be a difference in sedimentary processes under rough or storm weather conditions; (3) investigation of the interactions between hydrodynamics and micro-topography (e.g., ripples). Micro-topography formation and destruction are common during ESWS (Zhang et al., 2016). This micro-topography can greatly increase bottom friction (Ke et al., 1994), which can slow current velocities and tidal wave propagation (Friedrichs and Madsen, 1992; Le Hir et al., 2000). Thus this enhanced bottom friction could increase turbulence within the near-bed region (Nezu and Nakagawa, 1993) and possibly bed-level change. Therefore, there is a need to undertake integrated and high-resolution measurements of currents, waves, SSCs, bed-level changes, and micro-topography during ESWS to better understand their interactions; (4) smaller instrument measurement volumes and standoff distances are required to facilitate *in situ* measurements in extremely shallow-water environments to allow improved parameterization of turbulence and sediment transport; (5) examination of the effects of sediment transport processes during ESWS on biogeochemical cycling. ESWS are usually characterized by high SSCs (Gao, 2010), which are rich in trace metals, nutrients, organic carbon, and anthropogenic contaminants (Dyer et al., 2000; Grabowski et al., 2011). Thus, such large and frequent erosion and accretion during ESWS are likely to play an important role in biogeochemical cycling.

6. Conclusions

Integrated field measurements of current velocities, waves, SSCs, and bed-level changes on an intertidal flat have quantified the hydrodynamic and sediment erosion–accretion processes during ESWS close to the seabed. Our major findings and their implications are as follows.

(1) The τ_{cw} values during ESWS in the initial flood stage were greater than the τ_{cr} values, and the τ_{cw} values during ESWS in the post-ebb stage were less than the τ_{cr} values. These differences in hydrodynamics led to strong erosion and accretion during ESWS in the flood and ebb stage of a tide, respectively. Relatively weak erosion occurred during RDWS in almost all tidal cycles. This indicated a large difference in sediment dynamics between ESWS and RDWS.

(2) Bed-level changes during ESWS were three times greater than during RDWS in a corresponding tide, and the rate of change was an order of magnitude higher than during RDWS. These larger and more rapid changes occurred because τ_{cw} values during ESWS were, on average, two times higher than during RDWS at the flood stage, and at the ebb stage τ_{cw} values were just half of the average τ_{cw} value during RDWS. These bed-level changes occurred even though ESWS made up only 10% of the entire tidal cycle.

(3) ESWS occur twice in every tide. Given that large bed shear stresses and bed-level changes were associated with ESWS, this indicated that ESWS has an important influence on morphological changes on intertidal flats.

(4) Our results demonstrated that ESWS have an important control on near-bed hydrodynamics that influence sediment dynamics and morphological changes. Thus further investigations into the relationships between hydrodynamics, micro-topography, and sediment transport processes during ESWS under a range of conditions will be an important area of future research for estuarine scientists.

Acknowledgements

We thank Dezhi Chen and Qingguang Zhu for their help with the fieldwork on the Rudong intertidal flat in the Jiangsu coast, China. Special thanks are extended to Chunyan Li and Fang Cao for their helpful suggestions during the preparation and revision of this manuscript. This work was supported by the National Natural Science Foundation of China (Grant Nos. 41576090 and 41625021), the Jiangsu Special Program for Science and Technology Innovation (Grant No. HY2017-2), State Key Laboratory of Marine Geology, Tongji University (Grant No. MG201906), and the Laboratory for Marine Geology, Qingdao National Laboratory for Marine Science and Technology (Grant No. MGQNLM-TD201807).

Appendix A. Calculation of bottom shear stress

The wave orbital velocity $\widehat{U}_\delta$ [m/s] at the edge of the wave boundary layer was estimated from the following equation:

$$\widehat{U}_\delta = \frac{\pi H}{T\sinh(2\pi h/L)} \tag{A1}$$

where H is the wave height [m], T is the wave period [s], L [$=(gT^2/\pi)\tanh(2\pi h/L)$] is the wavelength [m], g is the acceleration due to gravity [9.81 m/s^2], and h is the water depth [m].

The wave-related bottom shear stress τ_w [N/m^2] was estimated as follows (van Rijn, 1993):

$$\tau_w = \frac{1}{2}\rho_w f_{wr}\widehat{U}_\delta^2 \tag{A2}$$

where ρ_w is seawater density [1028 kg/m^3] and f_{wr} is the wave friction coefficient [–], which was calculated as follows (Soulsby, 1997):

$$f_{wr} = 0.237r^{-0.52} \tag{A3}$$

$$r = A/k_s \tag{A4}$$

where r is the relative roughness [–], A is the semi-orbital excursion (= $\widehat{U}_\delta T/2\pi$ [m]), and k_s is the Nikuradse grain roughness (2.5 d_{50} [m]; d_{50} is the median grain size; Whitehouse et al., 2000).

During calm weather, the velocity structure in the bottom boundary layer is considered to exhibit a logarithmic velocity profile (LP method) (e.g., Soulsby and Dyer, 1981; Dyer, 1986; Grant and Madsen, 1986; Andersen et al., 2007; Salehi and Strom, 2012; Zhang et al., 2016) and is expressed as follows (Dyer, 1986; Whitehouse et al., 2000):

$$u = \frac{u_*}{k}\ln\left(\frac{z}{z_0}\right) \tag{A5}$$

where u is the measured velocity at height z above the bed [m/s], k is the von Karman's constant (0.4), z_0 is the bed roughness length related to the Nikuradse grain roughness k_s ($z_0 = k_s/30$ [m]; Whitehouse et al., 2000), and u_* is the friction velocity [m/s]. Variation in u during ESWS was obtained from the EMCM instrument, and variation in u during RDWS was obtained from the ADV instrument.

The current-related bottom shear stress τ_c [N/m^2] was estimated from the friction velocity u_*:

$$\tau_c = \rho_w u_*^2 \tag{A6}$$

where ρ_w is the density of seawater [kg/m^3].

We used the current–wave interaction model (Grant and Madsen, 1979) to calculate the bed shear stress due to combined current–wave action

(τ_{cw}), which is described as follows:

$$\tau_{cw} = \sqrt{(\tau_w + \tau_c\ |\cos\varphi_{cw}|)^2 + (\tau_c \sin\varphi_{cw})^2} \tag{A7}$$

where φ_{cw} is the angle between the wave and current directions. The current direction was obtained from the ADV and EMCM instruments. The wave direction was estimated by a standard PUV method (available at http://www.nortekusa.com/usa/knowledge-center/table-of-contents/waves). We computed wave directional spectra from ADV data by combining horizontal velocities and pressure data from the ADV data.

Appendix B. Theory of sediment erosion and accretion

Intratidal erosion and accretion typically depend on the balance between erosional F_e [kg/m^2/s] and depositional flux F_d [kg/m^2/s] (Winterwerp and van Kesteren, 2004; Lumborg, 2005). Net erosion occurs when $F_e > F_d$, and net accretion when $F_e < F_d$. Based on the work of Partheniades (1965) and Winterwerp and van Kesteren (2004), erosional and depositional fluxes can respectively be expressed as follows (Owen, 1977; Whitehouse et al., 2000):

$$F_e = \begin{cases} M_e(\tau_{cw} - \tau_{cr}), & \tau_{cw} > \tau_{cr} \\ 0, & \tau_{cw} \leqslant \tau_{cr} \end{cases} \tag{B1}$$

$$F_d = (SSC)w_{50} \tag{B2}$$

where τ_{cw} is the combined bed shear stress due to current–wave action [N/m^2], M_e is the erodibility parameter [m/Pa/s] known as the erosion constant, SSC is the near-bed concentration of suspended sediment]kg/m^3], w_{50} is the median settling velocity of suspended sediment in the water column [m/s], and τ_{cr} is the critical bed shear stress for erosion [N/m^2] obtained using the approach developed by Shields (1936), Miller et al. (1977), and Soulsby (1997):

$$\tau_{cr} = \theta_{cr} g(\rho_s - \rho_w) d_{50} \tag{B3}$$

$$\theta_{cr} = \frac{0.30}{1 + 1.2D_*} + 0.055[1 - exp(-0.02D_*)] \tag{B4}$$

$$D_* = \left[\frac{g(s-1)}{\nu^2}\right]^{\frac{1}{3}} \mathrm{d}_{50} \tag{B5}$$

where θ_{cr} is the threshold Shields parameter [–], ρ_s is the grain density [2650 kg/m^3], D_* is the dimensionless grain size [–], s (ρ_s/ρ_w) is the ratio of grain density to seawater density [2.58], and ν is the kinematic viscosity of seawater [1.36×10^{-6} m^2/s].

References

Andersen, T.J., Pejrup, M., Nielsen, A.A., 2006. Long-term and high resolution measurements of bed level changes in a temperate, microtidal coastal lagoon. Mar. Geol. 226, 115–125.

Andersen, T.J., Fredsoe, J., Pejrup, M., 2007. In situ estimation of erosion and deposition thresholds by Acoustic Doppler Velocimeter (ADV). Estuar. Coast. Shelf Sci. 75, 327–336. https://doi.org/10.1016/j.ecss.2007.04.039.

Balke, T., Bouma, T.J., Horstman, E.M., Webb, E.L., Erftemeijer, P.L., Herman, P.M., 2011. Windows of opportunity: thresholds to mangrove seedling establishment on tidal flats. Mar. Ecol. Prog. Ser. 440, 1–9.

Barbier, E.B., 2013. Valuing ecosystem services for coastal wetland protection and restoration: progress and challenges. Resources 2, 213–230.

Bayliss-Smith, T.P., Healey, R., Lailey, R., Spencer, T., Stoddart, D.R., 1979. Tidal flows in salt marsh creeks. Estuar. Coast. Mar. Sci. 9 (3), 235–255.

Bouma, T.J., van Belzen, J., Balke, T., van Dalen, J., Klaassen, P., Hartog, A.M., Herman, P.M.J., 2016. Short-term mudflat dynamics drive long-term cyclic salt marsh dynamics. Limnol. Oceanogr. 61 (6), 2261–2275.

Downing, J.P., Sternberg, R.W., Lister, C.R.B., 1981. New instrumentation for the investigation of sediment suspension processes in the shallow marine environment. Mar. Geol. 42 (1–4), 19–34.

Dyer, K.R., 1986. Coastal and Estuarine Sediment Dynamics. John Wiley and Sons.

Dyer, K.R., 1989. Sediment processes in estuaries: future research requirements. J. Geophys. Res. 94 (C10), 14327–14339.

Dyer, K.R., Christie, M.C., Feates, N., Fennessy, M.J., Pejrup, M., van der Lee, W., 2000. An investigation into processes influencing the morphodynamics of an intertidal mudflat, the Dollard estuary, the Netherlands: I. Hydrodynamics and suspended sediment. Estuar. Coast. Shelf Sci. 50 (5), 607–625. https://doi.org/10.1006/ecss.1999.0596.

Eisma, D., 1998. Intertidal Deposits: River Mouth, Tidal Flats, and Coastal Lagoons. CRC Press, pp. 459.

Fagherazzi, S., Hannion, M., D'Odorico, P., 2008. Geomorphic structure of tidal hydrodynamics in salt marsh creeks. Water Resour. Res. 44 (2).

Fagherazzi, S., Mariotti, G., 2012. Mudflat runnels: evidence and importance of very shallow flows in intertidal morphodynamics. Geophys. Res. Lett. 39 (14), L14402.

Feddersen, F., Gallagher, E.L., Guza, R.T., Elgar, S., 2003. The drag coefficient, bottom roughness, and wave-breaking in the nearshore. Coast. Eng. 48 (3), 189–195.

Friedrichs, C.T., Madsen, O.S., 1992. Nonlinear diffusion of the tidal signal in frictionally dominated embayments. J. Geophys. Res. Oceans 97 (C4), 5637–5650.

Gao, S., 2010. Extremely shallow water benthic boundary layer processes and the resultant sedimentological and morphological characteristics. Acta Sedimentol. Sin. 28 (5), 926–932 (in Chinese).

Grabowski, R.C., Droppo, I.G., Wharton, G., 2011. Erodibility of cohesive sediment: the importance of sediment properties. Earth Sci. Rev. 105 (3), 101–120.

Grant, W.D., Madsen, O.S., 1979. Combined wave and current interaction with a rough bottom. J. Geophys. Res. 84, 1797–1808.

Grant, W.D., Madsen, O.S., 1986. The continental-shelf bottom boundary layer. Annu. Rev. Fluid Mech. 18 (1), 265–305.

Hu, Z., Wang, Z.B., Zitman, T.J., Stive, M.J.F., Bouma, T.J., 2015. Predicting long-term and short-term tidal flat morphodynamics using a dynamic equilibrium theory. J. Geophys. Res. Earth Surf. 120, 1803–1823. https://doi.org/10.1002/2015JF003486.

Hughes, Z.J., 2012. Tidal channels on tidal flats and marshes. In: Principles of Tidal Sedimentology. Springer, Netherlands, pp. 269–300.

Janssen-Stelder, B., 2000. The effect of different hydrodynamic conditions on the morphodynamics of a tidal mudflat in the Dutch Wadden Sea. Cont. Shelf Res. 20, 1461–1478.

Kautsky, N., Evans, S., 1987. Role of biodeposition by Mytilus edulis in the circulation of matter and nutrients in a Baltic coastal ecosystem. Mar. Ecol. Prog. Ser. 201–212.

Ke, X.K., Collins, M.B., Poulos, S.E., 1994. Velocity structure and sea-bed roughness associated with intertidal (sand and mud) flats and salt-marshes of the Wash, UK. J. Coast. Res. 10 (3), 702–715.

Le Hir, P., Roberts, W., Cazaillet, O., Christie, M., Bassoullet, P., Bacher, C., 2000. Characterization of intertidal flat hydrodynamics. Cont. Shelf Res. 20, 1433–1459.

Li, P., Yang, S.L., Milliman, J.D., Xu, K.H., Qin, W.H., Wu, C.S., 2012. Spatial, temporal, and human-induced variations in suspended sediment concentration in the surface waters of the Yangtze Estuary and adjacent coastal areas. Estuar. Coast. 35, 1316–1327.

Lumborg, U., 2005. Modelling the deposition, erosion, and flux of cohesive sediment through Øresund. J. Mar. Syst. 56 (1), 179–193.

Lyne, V.D., Butman, B., Grant, W.D., 1990. Sediment movement along the US east coast continental shelf—I. Estimates of bottom stress using the Grant-Madsen model and near-bottom wave and current measurements. Cont. Shelf Res. 10 (5), 397–428.

MacVean, L.J., Lacy, J.R., 2014. Interactions between waves, sediment, and turbulence on a shallow estuarine mudflat. J. Geophys. Res. Oceans 119, 1534–1553. https://doi.org/10.1002/2013JC009477.

Mellor, G., 2002. Oscillatory bottom boundary layers. J. Phys. Oceanogr. 32 (11), 3075–3088.

Meziane, T., Tsuchiya, M., 2000. Fatty acids as tracers of organic matter in the sediment and food web of a mangrove/intertidal flat ecosystem, Okinawa, Japan. Mar. Ecol. Prog. Ser. 49–57.

Miller, M.C., McCave, I.N., Komar, P.D., 1977. Threshold of sediment motion under unidirectional current. Sedimentology 24, 507–527.

Nezu, I., Nakagawa, H., 1993. Turbulence in Open Channel Flows. IAHR Monograph. A.A.

Balkema, Rotterdam.
Nowacki, D.J., Ogston, A.S., 2013. Water and sediment transport of channel-flat systems in a mesotidal mudflat: Willapa Bay, Washington. Cont. Shelf Res. 60, S111–S124.
Owen, M.W., 1977. Problems in the modelling of transport, erosion, and deposition of cohesive sediments. In: In: Goldberg, E.D. (Ed.), The Ideas and Observations on Progress in the Study of the Seas Vol. 6. John Wiley and Sons Ltd., pp. 515–537 Ch. 12.
Partheniades, E., 1965. Erosion and deposition of cohesive soils. J. Hydraul. Div. Proc. ASCE 91 (HY1), 105–139.
Pethick, J.S., 1980. Velocity surges and asymmetry in tidal channels. Estuar. Coast. Mar. Sci. 11 (3), 331–345.
Postma, H., 1967. Sediment transport and sedimentation in the estuarine environment. In: Lauff, G.H. (Ed.), Estuaries. American Association for the Advancement of Science, pp. 158–179.
Ren, M.E., 1986. Tidal mud flat. In: Ren, M.E. (Ed.), Modern Sedimentation in the Coastal and Nearshore Zones of China. China Ocean Press, Beijing, pp. 78–127.
Ren, M.E., Zhang, R.S., Yang, J.H., 1985. Effect of typhoon no. 8114 on coastal morphology and sedimentation of Jiangsu Province PRC. J. Coastal Res. 1 (1), 21–28.
Salehi, M., Strom, K., 2012. Measurement of critical shear stress of mud mixtures in the San Jacinto estuary under different wave and current combinations. Cont. Shelf Res. 47, 78–92. https://doi.org/10.1016/j.csr.2012.07.004.
Shi, B.W., Yang, S.L., Wang, Y.P., Yu, Q., Li, M.L., 2014. Intratidal erosion and deposition rates inferred from field observations of hydrodynamic and sedimentary processes: a case study of a mudflat–saltmarsh transition at the Yangtze delta front. Continental Shelf Res. https://doi.org/10.1016/j.csr.2014.01.019.
Shi, B.W., Wang, Y.P., Yang, Y., Li, M.L., Li, P., Ni, W.F., Gao, J.H., 2015. Determination of critical shear stresses for erosion and deposition based on in situ measurements of currents and waves over an intertidal mudflat. J. Coastal Res 31, 1344–1356.
Shi, B.W., Wang, Y.P., Du, X.Q., Cooper, J.R., Li, P., Li, M.L., Yang, Y., 2016. Field and theoretical investigation of sediment mass fluxes on an accretional coastal mudflat. J. Hydro-environment Res. 11, 75–90.
Shi, B.W., Cooper, J.R., Pratolongo, P.D., Gao, S., Bouma, T.J., Li, G., Li, C., Yang, S.L., Wang, Y.P., 2017. Erosion and accretion on a mudflat: the Importance of very shallow-water effects. J. Geophys. Res. Oceans 122 (12), 9476–9499.
Shields, A., 1936. Application of similarity principles and turbulence research to bed-load movement. MittPreuss. Versuchsanstalt Wasserbau Schiffbau 26, pp. 5–24.
Soulsby, R., 1997. Dynamics of Marine Sands: A Manual for Practical Applications. Thomas Telford.
Soulsby, R.L., Dyer, K.R., 1981. The form of the near-bed velocity profile in a tidally accelerating flow. J. Geophys. Res. 86 (C9), 8067–8074.
Suykerbuyk, W., Bouma, T.J., Govers, L.L., Giesen, K., de Jong, D.J., Herman, P., van Katwijk, M.M., 2016. Surviving in changing seascapes: sediment dynamics as bottleneck for long-term seagrass presence. Ecosystems 19 (2), 296–310.
van Rijn, L.C., 1993. Principles of Sediment Transport in Rivers, Estuaries and Coastal Seas (2.7, 2.15–2.16 pp.). Aqua Publication, Amsterdam, the Netherlands.
Wang, X., Ke, X., 1997. Grain-size characteristics of the extant tidal flat sediments along the Jiangsu coast, China. Sed. Geol. 112 (1), 105–122.
Wang, A.J., Ye, X., Du, X.Q., Zheng, B.X., 2014. Observations of cohesive sediment behaviors in the muddy area of the northern Taiwan Strait, China. Cont. Shelf Res. 90, 60–69.
Wang, Y.P., Zhang, R., Gao, S., 1999. Velocity variations in salt marsh creeks, Jiangsu, China. J. Coast. Res. 15 (2), 471–477.
Wang, Y.P., Gao, S., Jia, J., Thompson, C.E., Gao, J., Yang, Y., 2012. Sediment transport over an accretional intertidal flat with influences of reclamation, Jiangsu coast, China. Mar. Geol. 291–294, 147–161.
Whitehouse, R., Soulsby, R., Roberts, W., Mitchener, H., 2000. Dynamics of Estuarine Muds: A Manual for Practical Applications. Tomas Telford Limited, Heron Quay, London.
Williams, J.J., Carling, P.A., Amos, C.L., Thompson, C., 2008. Field investigation of ridge-runnel dynamics on an intertidal mudflat. Estuar. Coast. Shelf Sci. 79 (2), 213–229. https://doi.org/10.1016/j.ecss.2008.04.001.
Winterwerp, J.C., van Kesteren, W.G.M., 2004. Introduction to the Physics of Cohesive Sediment in the Marine Environment. Elsevier, Amsterdam.
Wolman, M.G., Miller, J.P., 1960. Magnitude and frequency of forces in geomorphic processes. J. Geol. 68 (1), 54–74.
Xing, F., Wang, Y.P., Wang, H.V., 2012. Tidal hydrodynamics and fine-grained sediment transport on the radial sand ridge system in the southern Yellow Sea. Mar. Geol. 291, 192–210.
Yang, Y., Wang, Y.P., Gao, S., Wang, X.H., Shi, B.W., Zhou, L., Wang, D.D., Dai, C., Li, G.C., 2016. Sediment resuspension in tidally dominated coastal environments: new insights into the threshold for initial movement. Ocean Dyn. 66 (3), 401–417.
Ysebaert, T., Herman, P.M.J., Meire, P., Craeymeersch, J., Verbeek, H., Heip, C.H.R., 2003. Large-scale spatial patterns in estuaries: estuarine macrobenthic communities in the Schelde estuary, NW-Europe. Estuar. Coast. Shelf Sci. 57, 335–355. https://doi.org/10.1016/S0272-7714(02)00359-1.
Yu, Q., Wang, Y., Shi, B., Wang, Y.P., Gao, S., 2017. Physical and sedimentary processes on the tidal flat of central Jiangsu Coast, China: headland induced tidal eddies and benthic fluid mud layers. Cont. Shelf Res. 133, 26–36.
Zhang, Q., Gong, Z., Zhang, C.K., Zhou, Z., Townend, I., 2016. Hydraulic and sediment dynamics at times of very shallow water on intertidal mudflats: the contribution of waves. J. Coastal Res. 75, 507–511.
Zhang, H., Madsen, O.S., Sannasiraj, S.A., Chan, E.S., 2004. Hydrodynamic model with wave–current interaction in coastal regions. Estuar. Coast. Shelf Sci. 61 (2), 317–324.
Zhou, Z., Olabarrieta, M., Stefanon, L., D'Alpaos, A., Carniello, L., Coco, G., 2014. A comparative study of physical and numerical modeling of tidal network ontogeny. J. Geophys. Res. Earth Surf. 119 (4), 892–912.
Zhu, D.K., Ke, X., Gao, S., 1986. Tidal fiat sedimentation of Jiangsu coast. J. Oceanogr. Huanghai Bohai Seas 4 (3), 19–27 (in Chinese with English abstract).